Quantitative analysis of diffuse X-ray scattering in partially transformed 3C-SiC single crystals

Alexandre Boulle, D. Dompoint, I. Galben-Sandulache, D. Chaussende

Quantitative analysis of diffuse X-ray scattering in partially transformed 3C-SiC single crystals

A. Boulle[1], D. Dompoint[1], I. Galben-Sandulache[2], D. Chaussende[2]

[1] Science des Procédés Céramiques et de Traitements de Surface CNRS UMR 6638, ENSCI, 47 avenue Albert Thomas 87065 Limoges Cedex, France

[2] Laboratoire des Matériaux et du Génie Physique CNRS UMR 5628, Grenoble INP, Minatec, 3 parvis Louis Néel, BP 257, 38016 Grenoble Cedex 01, France

Abstract

The X-ray scattering of partially transformed 3C-SiC single crystals is considered in details. Extended diffuse scattering streaks, originating from stacking faults (SFs) lying in the {111} planes, are clearly observed in the wide-range reciprocal space maps. The intensity distribution along the diffuse streaks is simulated with a model including the contributions of the diffuse scattering originating from the SFs [based on the pioneering theoretical description given by Kabra *et al.* (*J. Mater. Sci.* **21**, 1654-1666 (1986))], the coherent scattering emanating from untransformed areas of the crystals, as well as all θ-dependent terms that affect the scattered intensity (the layer structure factor, the irradiated volume and the polarization of the beam). The quantitative simulation of the diffuse streaks reveals that the transformation occurs through the glide of partial dislocations and allows to derive the transformation level. It is shown that the 3C polytype is indeed unstable at high temperature. However, it is further shown that defect-free 3C-SiC single crystals remain stable at temperatures where it is known to be usually unstable (1900°C). The origin of this apparent stability is very likely of kinetic nature, *i.e.* the lack of crystalline defects inhibits the transformation.

1. Introduction

Among the more than 200 SiC polytypes, the cubic silicon carbide (3C-SiC) exhibits the highest electron mobility and isotropic electrical properties which make it the most desirable polytype for active device applications (Nagasawa *et al.*, 2008). However, despite decades of studies, the actual performances of 3C-SiC based devices have never reached the expected theoretical performances, mainly because of the too poor 3C-SiC crystals quality. Even in the best free-standing 3C-SiC wafers, the defect density still is much higher than in the high-quality commercial 4H or 6H-SiC wafers. It is now commonly admitted that this poor crystal quality originates from the high temperatures that are required to grow SiC (>1900°C) where the 3C phase is believed to be unstable (Knippenberg, 1963 ; Heine *et al.*, 1992 ; Limpijumnong & Lambrecht, 1998). A direct consequence of this instability is that the stacking fault (SF) energy is negative at these temperatures (Thomas *et al.*, 2008 ; Lindefelt *et al.*, 2003) which hence promotes the 3C-6H polytypic transition through the formation and expansion of a large number of SFs. The understanding of the physics underlying this phase transition is a key issue for the development of high-quality 3C-SiC single crystals.

The most important achievements in the understanding of the 3C-6H transition have been realized in the study of polycrystalline (powdered or compacted) samples mainly using high-resolution transmission electron microscopy (HR-TEM) as this technique allows a direct visualization of the stacking sequences and defects in the structure [see Jepps & Page (1983) and references therein]. It has also been shown that the transformation in such samples mainly occurs through fast transport mechanisms (e.g. surface or vapor phase diffusion) while much slower solid-state mechanisms are expected in the transformation of large single crystals (Jepps & Page, 1983). The conclusions drawn for polycrystalline samples can hence not be used in the study of single crystals. The first attempts to clearly identify the mechanism involved in the solid-state 3C-6H transition have been simultaneously performed by Jagodzinski (1971) and Krishna & Marshall (1971) both using X-ray diffraction (XRD)

rotation photographs. Both studies concluded that the transition occurs in the solid-state through a "layer-displacement" mechanism where a 3C stacking, ...ABCA[BC]ABC..., is transformed into a 6H stacking, ...ABCA[CB]ABC... . This re-stacking can be performed by local diffusional rearrangement of the Si and C atoms (in the layers indicated by the square brackets) according to a mechanism first proposed by Jagodzinski (1954) or by the *simultaneous* nucleation of three Schockley partials in three successive layers (Kabra *et al.*, 1986). The layer displacement mechanism has been suggested by Kabra *et al.* (1986) on the basis of XRD rotation photographs and simulations of the diffuse scattering induced by the SFs.

An alternative mechanism has been suggested by Ogbuji *et al.* (1981) in which three Shockley partial dislocations *successively*[1] transforms the initial 3C structure into ...ABCA|CABCA..., ...ABCAC|BCAB... and finally ...ABCACB|ABC... (the staking fault associated with the Shockley partial is indicated by the bar). At first sight the successive nucleation and growth of three *different* partials on three consecutive planes appears as a highly unlikely process. An elegant and physically sound explanation has been proposed by Pirouz and coworkers (Pirouz, 1989 ; Pirouz & Yang, 1993). In this process, a pinned partial dislocation, originating from the dissociation of a screw dislocation lying in a given (111) plane, acts as a Frank-Read source and a faulted plane is produced by the displacement of the partial dislocation. The successive plane is faulted by the *same* partial dislocation which underwent a double-cross-slip motion and this process is repeated one additional time in order to produce the desired 6H sequence. This mechanism is supported by TEM observations (Pirouz & Yang, 1993) as well as by *ab initio* simulations (Käckell *et al.*, 1999).

The purpose of the present article is to revisit the question of the 3C-6H transition mechanism by means of modern XRD techniques, in particular wide-range reciprocal space mapping associated with numerical simulations of the diffuse X-ray scattering (DXS). We shall show that a quantitative analysis

1 This is major difference as compared to the layer-displacement mechanism where the nucleation of three Shockley partials occurs in a single unit process.

of the DXS intensity profiles allows to unambiguously identify the mechanism involved in the 3C-6H transition, as well as to determine the transformation level. Details concerning data acquisition and data processing are given in section 2. In section 3 we describe in details the methodology used to model the DXS intensity distribution and all terms affecting the scattered intensity (layer structure factor, irradiated volume, polarisation) are discussed. Finally, in section 4 the transformation mechanisms and the influence of the crystal quality on the transformation level are discussed.

2. Experimental details

2.1 3C-SiC single crystals

In the present study we used 10 × 10 mm², 250 µm – thick, commercially available (001)-oriented 3C-SiC single crystals (HAST Corporation) grown by chemical vapor deposition on "undulant" (001) Si wafers (Nagasawa *et al.*, 2002 ; Nagasawa *et al.*, 2006). Three different type of crystals have been investigated: an untransformed 3C-SiC crystal and two partially transformed crystals with different initial transformation levels (0.6 and 1.6%). These crystals are then annealed between 1700 and 1900°C so as to further promote the 3C-6H transition. The annealing experiments are conducted under 600 mbar of argon. The surface of the sample is slightly graphitized upon annealing. The graphite layer is removed before XRD measurements.

The undulant (001) Si substrates exhibit trenches running parallel to the [1-10] direction resulting in an anisotropic fault distribution in the grown 3C-SiC crystals (Nagasawa *et al.*, 2002 ; Polychroniadis *et al.*, 2004 ; Boulle *et al.*, 2006 ; Boulle *et al.*, 2007). This orientation corresponds to the high SF density direction (Boulle *et al.*, 2006) and it turns out that the 3C-6H transition actually occurs along the [1-11] and [-111]. Conversely, no significant diffuse scattering was observed for the 90° equivalent orientation, indicating that the transformation does not occur along [111] and [-1-11]. All results presented below hence correspond to the orientation where the transformation is observed.

2.2 Wide-range reciprocal space mapping

Wide-range reciprocal space maps (RSMs) have been recorded on a home-made laboratory equipment based on a rotating Cu anode coupled with a four reflections Ge(220) monochromator and equipped with a curved position sensitive detector (PSD) with a 120° angular aperture operating in 8192-channels mode (that is an average channel size of ~0.015°). A five-movement sample holder allows precise sample positioning. The X-ray beam impinging on the sample is monochromatic (Cu $K\alpha_1$, $\Delta\lambda/\lambda=1.4\times10^{-4}$) and parallel in the detector plane ($\Delta\theta = 0.0033°$) with dimensions 10×0.1 mm^2 so that a large volume of the sample is analyzed which provides statistically significant averaged values. A detailed description of the set-up has been given elsewhere (Boulle *et al.*, 2001, 2002). A RSM represents the scattered intensity in a particular (Q_x, Q_z) plane, where Q_x and Q_z are the components of the scattering vector **Q** ($Q = 4\pi \sin\theta / \lambda$) in the film plane and perpendicular to it, respectively. In the following experiments, Q_x and Q_z have been set parallel to the [1-10] and the [001] directions of SiC.

The reciprocal lattice of 3C-SiC together with the incident wave vector $\mathbf{K}_0$ and the associated Ewald's sphere are represented in Fig. 1(a) (the Ewald's sphere is reduced to a 120°-wide arc so as to match the actual angular aperture of the PSD). When the incidence angle ω is varied between ω_0 and $\omega_0 + \Delta\omega$ the Ewald's sphere spans the range indicated by the shaded area, so that in one single ω-scan we record a very wide portion of the reciprocal space, including the (-113) and (002) reflections of 3C-SiC. Because we make use of a PSD, which is regularly gridded on the 2θ scale[2], the RSM can not be directly recorded as a function of the Q_x and Q_z coordinates (as is now commonly feasible on most commercial X-ray diffractometers and at synchrotron radiation facilities). Instead, the RSMs are recorded as a function of the scanning angles, ω and 2θ, which are then converted into the reciprocal

2 Strictly speaking, the PSD is not exactly regularly gridded on the 2θ scale. The discrepancy between the expected angular position of a counting channel and its actual position is known as the integral linearity of the counter and is accounted for using a suitable calibration procedure (Boulle *et al.*, 2002 ; Masson *et al.*, 2005).

lattice coordinates according to:

$$Q_x = 4\pi \sin\theta \sin(\omega - \theta)/\lambda$$

$$Q_z = 4\pi \sin\theta \cos(\omega - \theta)/\lambda$$

A schematic representation of the corresponding data mesh in the reciprocal space is depicted in Fig. 1(b). For representation purposes and further data processing (line scan extraction, etc.) the data set has to be interpolated so as to be regularly gridded in the (Q_x, Q_z) frame. This procedure is performed in two steps. Firstly the original data set is triangulated using a Delaunay triangulation scheme (Berg *et al.*, 2008). Secondly a (Q_x, Q_z) mesh is generated and the intensity at each node of the mesh is obtained by linear interpolation within the corresponding triangle.

The transitions between the different SiC polytypes are most easily understood when considering a hexagonal coordinate system where planes of corner-sharing [CSi_4] tetrahedrons are stacked along the $[001]_h$ direction, the in-plane edges of the tetrahedrons being parallel to $[100]_h$, $[010]_h$ and $[110]_h$ (the subscript 'h' refers to 'hexagonal') (Jepps & Page, 1984). In the case of the 3C-6H transition, we shall hence describe 3C-SiC using the usual three - layer hexagonal unit cell where the $[111]_c$ direction of the cubic unit-cell is parallel to the $[001]_h$ direction of the hexagonal unit-cell (Warren, 1969). The correspondence between the cubic and hexagonal reciprocal lattices is represented in Fig. 2(a). The row joining the (002) and the (-113) reflections in the cubic lattice, corresponds to the $[10L]_h$ row in the hexagonal lattice, so that these reflections are also written $(102)_h$ and $(105)_h$, respectively (we conform to the usual notation where the hexagonal Miller indices are written in upper case). Hereinafter we shall only make use of the hexagonal indices. Since we make use of a three-layer hexagonal unit cell, a given $(H\,K\,L)_h$ reflection corresponds to the $(H\,K\,2L)$ reflection in the actual 6H unit cell.

A typical RSM of a significantly transformed crystal (with a 5.2% transformation level) is shown in figure 2(b). A significant diffuse scattering intensity is recorded along the $[10L]_h$ row indicating the presence of planar defects lying in the hexagonal $(001)_h$ basal planes. Besides, the streak labeled 'PSD'

is due to the transmittance function of the PSD (Boulle *et al.*, 2002). This streak lies along the Ewald sphere as indicated by the dashed curves in Fig. 1, and it therefore makes an angle of 20.697° with the normal to the surface in the case of the $(102)_h$ reflection and 61.119° in the case of the $(105)_h$ reflection. It is worth recalling that this map has been recorded in the same amount of time than a single ω-scan without impairing the resolution which is set by the incident beam divergence, *i.e.* 0.0033° [except along the PSD streak where it is one order of magnitude worse (Boulle *et al*., 2002)].

We show in the following that the quantitative analysis, by means of numerical simulations, of the diffuse scattering intensity located along the $[10L]_h$ row allows to obtain a detailed information concerning the transformation mechanisms as well as the transformation level. For that purpose, there is an undeniable advantage in recording a full reciprocal space map since this allows to extract a line scan precisely located along the $[10L]_h$ row. We are hence immune to some sample misalignment errors (such as an unintentional ω-2θ offset for instance) that would dramatically affect the intensity obtained with a single scan, especially because the streak is extremely narrow in the direction perpendicular to $[10L]_h$. Moreover, in order to improve the counting statistics, when extracting the $[10L]_h$ scan we integrate the intensity in the direction perpendicular to $[10L]_h$ so as to include all the intensity contained in the diffuse streak [in the direction perpendicular to the (Q_x, Q_z) plane the integration is ensured by the divergence of the beam (Boulle *et al*., 2002)].

3. X-ray diffraction from transformed 3C-SiC crystals

The study of one-dimensional disorder in crystals is a longstanding problem which started in the late 1930s (Landau, 1937; Lifshitz, 1937) and which still remains an active research area. The approach which we rely on in this work is based on the concept of non-random faulting introduced to analyze the 2H-6H transition (Pandey *et al.*, 1980) and extended later to the 3C-6H transition (Kabra *et al.*, 1986). However, up until now it was not used in a quantitative way in the sense that it did not permit to fit

experimental diffuse scattering profile in order to obtain, for instance, the transformation level of crystals undergoing the 3C-6H transition. The main reason for that was the lack of available high quality XRD data. In the following we shall make use of this approach to simulate the diffuse scattering profiles obtained from wide-range reciprocal space mapping experiments. Particular emphasis is laid on the description of the experimental factors affecting the shape of the intensity distribution.

Within the framework of the kinematical theory of diffraction (Warren, 1969), the intensity distribution along the $[10L]_h$ row can be written:

$$I(L) = k \cdot P V \int dL' \cdot R(L') I_s(L - L') + b \qquad (1)$$

where the scale factor k and the background b are constants for a given set of experimental conditions (incident beam intensity, counting time...). P and V are the polarization and the irradiated volume, respectively. $I_s(L)$ is the intensity diffracted by the sample which has to be convoluted with the resolution of the diffractometer $R(L)$. The resolution of the diffractometer has been studied in details elsewhere (Boulle *et al.*, 2002). In present case it is very well described by a Gaussian function with a FWHM (full width at half-maximum) = 0.006 close to $L = 2$, and FWHM = 0.01 close to $L = 5$, as estimated from the width of the coherent peaks of an untransformed 3C-SiC crystal. It should be noted however that this broadening has a noticeable effect only in the case of very narrow peaks (as those emanating from a perfect single crystal). The broad diffuse scattering intensity distribution remains unaffected by the resolution of diffractometer. Finally, it must be mentioned that in the case of a significant beam divergence, specific correction must be applied to the measured scattered intensity in order to recover the actual intensity distribution along the diffuse streaks (Pandey *et al.*, 1987). These corrections originate from the fact that in such a case the measured intensity at given incidence angle actually results from the integration of the diffuse streak over a length determined by the divergence of the beam. In the present case, because of the excellent beam collimation (0.0033°) such corrections are not necessary.

3.1 Diffuse scattering

As mentioned earlier, the intensity diffracted from a partially transformed crystal is calculated by means of the approach developed by Kabra *et al.* (1986). Within this formalism the intensity distribution along the $[10L]_h$ row can be written (see also Holloway, 1969)

$$I_t(L) = C\psi^2 I_c + 2(1-C)\psi^2 \times \Re\left\{\frac{1}{2} + \frac{\sum_{n=1}^{N-1}\sum_{m=0}^{n-1} a_{N-m} J_{n-m} \exp\left[-2\pi i (N-m) L/3\right] - a_0 J_0}{\sum_{n=0}^{N} a_n \exp\left[-2\pi i n L/3\right]}\right\} \qquad (2)$$

where L is the Miller index corresponding to the 3C hexagonal unit-cell. The first term on the right-hand side of equation (2) is the coherent part of the scattered intensity, the intensity of which is modulated by a Debye-Waller – like factor ($C \in [0,1]$) which depends on the faulting structure (*e.g.* on the transformation mechanism) and the defect density. The coherent intensity, I_c, is described in the next section. The term ψ^2 is proportional to the squared structure factor, f^2, of a single "SiC" layer and to the intensity distribution in the directions perpendicular to $[10L]_h$ (Warren, 1969). Since in the present case the intensity is integrated in the direction perpendicular to $[10L]_h$, ψ^2 reduce to Af^2, where A is the crystal's cross-section in the directions perpendicular to $[10L]_h$. The second term on the right hand side of equation (2) is the diffuse scattering due to the presence of faults. The main advantage of this formulation is that it does not necessitate an explicit resolution of difference-equation (Holloway, 1969), but it only requires the expression of the pair correlation function, J_m, and the coefficients of the difference-equation, a_n (although this remains a challenging and cumbersome task in many cases). In the case of the 3C-6H transition, both J_m and a_n can be calculated analytically assuming a certain transition mechanism and therefore a particular faulting structure.

For the dislocation-based mechanism it turns out that $C = 0$ (*i.e.* the intensity of the coherent peak is 0) and $N = 6$, and the coefficients J_m and a_n are given by Kabra *et al.* (1986, p. 1657) :

$a_0 = -\tau^2$; $J_0 = 1$

$a_1 = -\omega\tau(1-\tau)$; $J_1 = (-2\tau + \tau^2\omega^2 + \omega)/D_1$

$a_2 = 0$; $J_2 = (\tau + \omega^2 + \tau^2\omega)/D_1$

$a_3 = 0$; $J_3 = (1-\tau)^2/D_1$

$a_4 = 0$; $J_4 = (1-\tau)(\omega - 2\tau\omega + \tau)/D_1$

$a_5 = -\omega(1-\tau)$; $J_5 = \{(1-\tau)[(\omega^2(1-3\tau) + 2\tau(\omega - \tau)] - \tau^2(1+2\tau)\}/D_1$

$a_6 = 1$ and $\omega = \exp(2\pi i/3)$, $D_1 = (1+\tau)^2 + 2\tau$,

where τ is the transformation level ($\tau = 0$ for the 3C phase and $\tau = 1$ for the 6H phase). The corresponding DXS profile [computed with the above coefficients and equations (1-2) and $\tau = 0.1$] is displayed in Fig. 3.

For the layer-displacement mechanism we have $C = [(1+2\tau)/(1+5\tau)]^2$ and $N = 5$. The expressions of J_m and a_n are not explicitly given in the above-mentioned reference. However, they can be deduced using the approach of Lele (1980) which holds in the case where one of the roots of the difference-equation has unit modulus. We obtain

$a_0 = \tau\omega^2$; $J_0 = [6\omega^2\tau + 3\tau^2(1 + \omega + 8\omega^2)]/D_2$

$a_1 = \tau\omega$; $J_1 = [-3\omega^2\tau + 3\tau^2(\omega - 4\omega^2 - 2)]/D_2$

$a_2 = \tau$; $J_2 = [3\tau^2(1-\omega)^2]/D_2$

$a_3 = \tau\omega^2$; $J_3 = [3\tau^2(1 + \omega - 2\omega^2)]/D_2$

$a_4 = \tau\omega$; $J_4 = [3\tau^2(\omega + \omega^2 - 2)]/D_2$

$a_5 = 1$ and $D_2 = \omega^2(1+5\tau)^2$.

An important assumption made in deriving equation (2) is that the whole crystal is transformed simultaneously. However, considering the very large lateral dimensions of the crystals (10×10 mm^2) this is very unlikely to happen. Moreover this assumption is contradictory with the analysis, using

Raman scattering, of similar 3C-SiC crystals undergoing the 3C-6H transformation which proved that the transformation is initiated at the surface and then propagates into the crystal volume (Yoo & Matsunami, 1991; Püsche *et al.*, 2004). In the volume probed with the X-ray beam both transformed and untransformed areas certainly co-exist so that we finally write the intensity scattered from the sample as

$$I_s = x_t I_t + (1 - x_t) I_c \tag{3}$$

where x_t is the volume fraction of transformed material.

3.2 Coherent scattering

Narrow and intense Bragg (coherent) peaks may appear in the $[10L]_h$ scan, either as a consequence of a non-zero Debye-Waller factor in equation (2) or as a consequence of the existence of untransformed regions in the crystal, equation (3). All previous studies on this type of 3C-SiC single crystals (Boulle *et al.*, 2006 ; Boulle *et al.*, 2009) revealed that the size of the domains over which diffraction is coherent (mosaic domains) is larger or close to the coherence length of the diffractometer (the inverse of the resolution). This result is in good agreement with the derivation of equation (2) which explicitly assumes infinite crystals, *i.e.* there should be no finite-size – induced broadening effects. In the following the mosaic domains have been assimilated to cubes with edge length D. The calculation has been performed within the framework of the kinematical theory of diffraction using the formalism described by Boulle, Conchon & Guinebretière (2006). Since the coherent peaks emanate from perfect regions of the crystal, the calculation can as well be carried out within the framework of the dynamical theory of diffraction (Authier, 2001). The intensity profile corresponding to the coherent diffraction from an untransformed region (assuming cubes with D = 6 μm) is depicted in Fig. 3 for the range L = 1.5 – 5.5. The coherent intensity is obviously not affected by the transformation level of the crystal, so that the Bragg peaks are extremely narrow and exactly located at L = 2 and L = 5, whereas they are

significantly broadened and shifted towards higher L values in the diffuse intensity distribution (in agreement with the initial calculation of Kabra *et al.* (1986)). Moreover, the DXS profile exhibits a significant intensity contribution between the Bragg peaks (which is obviously not present in the coherent intensity distribution) which corresponds to the diffuse streaks observed in the RSMs. Finally, it should be noted that even in the most transformed crystals analyzed in this work, the mosaic domain size still remains as large as 300-500 nm (as estimated from the width of the Bragg peaks), which is largely sufficient to yield negligible effects on the DXS profiles. However, this effect must be taken into account in the calculation of the coherent profile.

3.3 The layer structure factor

Since we are scanning wide regions of the reciprocal space, the layer structure factor can clearly not be assumed as being a constant across the whole range of L. We make use of the classical description of close-packed structures where the Si atoms form a hexagonal close-packed layer whereas the C atom occupies the tetrahedral void with coordinates (1/3, 2/3, z). In the ideal 2H structure $z_{2H} = 1/8$, so that in the three-layers hexagonal structure we have $z_{3C} = (2/3)z_{2H} = 1/12$. The layer structure factor writes

$$f = f_{Si} + f_C \exp\left[2\pi i\left(\frac{H}{3} + \frac{2K}{3} + L z_{3C}\right)\right] \tag{4}$$

The atomic scattering factors f_{Si} and f_C depend on the scattering angle θ and are computed using the method of Waasmaier & Kirfel (1995). Finally, considering the $[10L]_h$ row and applying Bragg's law, the scattering angle is related to the Miller index L through

$$\theta = \mathrm{asin}\left(\frac{\lambda}{2a\sqrt{3}}\sqrt{8 + L^2}\right) \tag{5}$$

where a is the cell parameter of 3C-SiC, a = 4.359 Å. The evolution of the squared structure factor is depicted in Fig. 3 for the range L = 1.5 – 5.5.

3.4 The irradiated volume and polarization

We finally consider the effect of the irradiated volume and the polarization of the X-ray beam. Let us first consider the intensity dI, diffracted by a volume element $dV = Sdz$, located at a depth z below the surface of the crystal, Fig. 4. The area S is related to the X-ray beam cross section S_0 and to the incidence angle ω according to $S = S_0 / \sin \omega$. Making use of Beer-Lambert's law we have

$$dI \propto I_0 \exp\left[-\mu(l_1+l_2)\right] dV \tag{6}$$

where I_0 is the incident beam intensity, μ is the linear absorption coefficient and $l_1 + l_2$ is the path length of the beam within the crystal.

The integration of equation (6) over the thickness of the crystal t yields an effective (*i.e.* accounting for absorption) irradiated volume

$$V = \frac{S}{\mu} \frac{\sin(\theta+\phi)}{\sin(\theta+\phi)+\sin(\theta-\phi)} \left(1 - \exp\left\{-\mu t \left[\frac{1}{\sin(\theta+\phi)} - \frac{1}{\sin(\theta-\phi)}\right]\right\}\right) \tag{7}$$

where $\phi = \theta - \omega$ is the asymmetry angle. Inspection of Fig. 2b allows to write ϕ as a function of the Miller index L :

$$\phi = \operatorname{asin}\left(\frac{L-2}{\sqrt{8+L^2}} \sin\psi\right) \tag{8}$$

and θ is given by equation (5).

The polarization of the beam impinging on the detector is determined by the different Bragg reflections encountered. Whereas the intensity of the σ – component remains constant, the intensity of the π– component is reduced by a factor $\cos^2\theta$ at each reflection with angle θ (Warren, 1969). Since we are using a four-reflection Ge(220) monochromator, the final polarization factor can be written

$$P = \frac{1+\cos^8\theta_{\mathrm{Ge(220)}} \cos^2\theta}{2} \tag{9}$$

The variations of V and P within the L = 1.5 – 5.5 range are plotted in Fig. 3. It can be seen that the

irradiated volume varies rapidly (more than a factor of 2) in the range L = 1.5 – 3.5, whereas the polarization has more limited influence.

From the previous calculations it appears that the diffuse scattering alone [as given by equation (2)] is not sufficient to accurately describe the actual intensity distribution along the $[10L]_h$ row. The coherent scattering must be taken into account [equation (3)] as well as the different θ-dependent terms (P, V and f^2) that affect the scattered intensity.

4. Application

4.1 Fitting methodology

The scattered intensity distribution is calculated using equations (1-9). The computer program has been written using the Python programming language[3] together with the SciPy scientific library[4]. The scale factor k (including all constant terms) and the background b are determined from the maximum and minimum intensity in the experimental $[10L]_h$ scan, respectively. The remaining parameters are the size of the mosaic domains D, the volume fraction of transformed material x_t and the level of transformation in the transformed regions τ. The overall transformation level is given by $x_t\tau$. The size of the mosaic domains is straightforwardly deduced from the width of the coherent peak so that the only free parameters in the fitting procedure are x_t and τ. Let us examine how these parameters affect the intensity distribution.

Fig. 5 shows the superposition of an experimental and a calculated curve (together with the coherent and diffuse components of the scattered intensity) in the vicinity of the L = 2 peak, where it can be seen that the model perfectly fits the data in the range of L considered. As expected from equation (3) the volume fraction of transformed material only affects the relative intensity of the diffuse and coherent components. The value of x_t is hence simply obtained by matching the coherent/diffuse intensity ratio.

3 http://www.python.org/
4 http://www.scipy.org/

The transformation level τ only affect the shape of the diffuse intensity distribution, as illustrated by the red curves. It turns out that the diffuse scattering is extremely sensitive to this latter parameter: the overall shape and the position of the maxima in the diffuse scattering curve are significantly affected by the transformation level, so that this parameter is easily obtained by fitting the diffuse part of the scattering profile.

Finally it should be noticed that since we are using a gas-filled PSD the intensity of the beam impinging on the counter should in principle not exceed ~ 3000 counts/s (in our case), otherwise the counting linearity is lost. Despite of that, we preferred not to use beam attenuators, even close to the Bragg peaks, since in such a case we would attenuate a whole portion of the reciprocal space and not only the region of high intensity. It turned out that close to the $L = 5$ peak the detector often saturates (especially for high-quality crystals), *i.e.* the intensity exceeds ~3000 counts/s, which leads to an underestimation of the peak intensity in its close vicinity. Therefore, although the $L = 5$ peak should exhibit a higher intensity, its measured intensity is lower than the $L = 2$ peak. For that reason, the region close to the $L = 5$ peak is not used in the fitting procedure.

4.2 The transformation mechanism

The experimental and simulated $[10L]_h$ scans of a partially transformed 3C-SiC single crystal are reported in Fig. 6. Let us first consider the raw (non-annealed) crystal, Fig. 6(a), where the simulation is performed assuming either the dislocation-based mechanism (full line) or the layer-displacement mechanism (dashed line). It can be concluded that the layer-displacement mechanism is unable to correctly describe the experimental data (see for instance the features pointed by the arrows, which are on the contrary very well reproduced with dislocation-based mechanism). It can hence be concluded that the 3C-6H transition takes place by the glide of partial dislocations. The overall transformation level is estimated to $x_t\tau = 1.6\%$. The annealing at high temperature (1700°C during 5 hours) further

promotes the 3C-6H transition, Fig. 6(b). This confirms that the 3C polytype is indeed unstable at high temperatures, since the overall transformation level is increased to $x_t\tau = 5.2\%$.

At first sight it might look surprising that, although we are using the same theoretical basis, our conclusions concerning the transformation mechanism are opposite to those of Kabra *et al.* (1986). This can be understood as follows. Firstly, they based their conclusions on the existence in their rotation photographs of narrow and intense peaks, so that (according to section 3.1) the only possible mechanism is the layer-displacement mechanism which is indeed characterized by a non-zero Debye-Waller factor. Contrarily to Kabra *et al.*, we included in the simulation the coherent scattering emanating from untransformed regions of the crystal so that the existence of a coherent peak is not a relevant criteria in our case. It is hence very likely that the narrow and intense peaks observed by Kabra *et al*. were also due to untransformed parts of their crystals. Secondly, since they were using rotation photographs (it must be borne in mind that their work goes back to the 1980s), they were unable to access the fine structure of the diffuse scattering. It appears, Fig. 6(a), that a detailed inspection of the fine structure of the diffuse scattering is mandatory to be able to conclude about the transformation mechanism.

Let us briefly discuss both transformation mechanisms from the point of view of the faulting probabilities. In the case of the dislocation-based mechanism the initial 3C-type stacking, ABCABCABC, is first transformed (with probability α) into $\underline{\text{ABCAC}_1}|\underline{\text{B}_2}\text{CAB}$ by means of the double-cross-slip process (the underlined symbols represent the 6H unit cell)[5]. In this first configuration, after the layer B_2, there is no guarantee that the 6H unit cell will repeat (*i.e.* that B_2 will be followed by an A_3 layer) since this implies the double-cross-slip motion to occur a second time (with the same probability) so as to yield $\underline{\text{ABCACB}_2}|\text{A}_3\text{BC}$. It is striking that, although it has been introduced a few years before, the probability tree derived by Kabra *et al.* (p1657) exactly corresponds to the

5 For convenience we here make use of the $A_iB_jC_k$-type stacking symbols, introduced by Pandey (1984), which are used to construct the probability trees in Kabra *et al.* (1986).

dislocation-based mechanism later developed by Pirouz (1989). On the contrary, in the case of the layer-displacement mechanism, the initial 3C-type stacking is directly transformed (with probability β) into $\underline{ABCA[CB_2]}A_3BC$, *i.e.* the layer B_2 is necessarily followed by an A_3 layer which ensures at least three more layers of 6H type [p1659 in Kabra *et al.* (1986)]. The present work hence validates the initial calculation of Kabra *et al.* and provides an unambiguous determination of the transformation mechanism.

4.3 Influence of initial crystal quality

Two additional crystals, with an improved initial crystal quality have been investigated. Sample 2 and sample 3 are characterized by a $x_t\tau$ = 0.6% [Fig. 7(a)] and $x_t\tau$ = 0.004% [Fig. 7(c)] initial transformation level, respectively (to be compared with sample 1 for which $x_t\tau$ = 1.6%). In both cases, the dislocation-based model fits the data fairly well which further confirms the nature of the transformation mechanism[6]. Sample 2 has been annealed at a higher temperature than sample 1 (1800°C during 5h), in order to increase the transformation kinetics as compared to sample 1. Similarly, sample 3 has been annealed successively at 1800°C during 2 h and 1900°C during 1h. Surprisingly, it turned out that, despite the higher temperatures, sample 2 and sample 3 were less transformed than sample 1. Sample 2, Fig. 7(b), exhibits an overall transformation level $x_t\tau$ = 3.75%, whereas sample 3 remained absolutely unchanged ($x_t\tau$ = 0.004%), Fig 7(d). In other words, the stability of 3C-SiC at high temperatures is directly dependent on its initial quality: lowering the crystal quality results in a lower high-temperature stability. This simple result indicates that, although the 3C polytype is unstable at high temperatures, the transformation is limited by the nucleation of crystalline defects (*i.e.* dislocations or stacking faults in the present case). This is in contrast with the study of polycrystalline samples (Jepps & Page, 1983) which systematically undergo the 3C-6H transition for

6 The model fits the data fairly well, excepted at L = 4 where a very weak and narrow peak sometimes appears, the origin of which is not completely understood to date.

temperatures > 1600°C. This discrepancy probably arises from the presence of surfaces and grain boundaries which, in the case of polycrystalline materials, act as a source of planar defects necessary for the transformation. This proves that it should be possible to grow large 3C-SiC single crystals at high temperatures, provided that crystalline defects are not introduced during growth.

5. Conclusions

The X-ray scattering from partially transformed 3C-SiC crystals has been quantitatively analyzed using wide-range reciprocal space mapping. $[10L]_h$ scans extracted from the maps have been simulated with a model including the diffuse scattering originating from the defect structure in the transformed crystals, the coherent scattering emanating from untransformed areas of the crystals, as well as all θ-dependent terms that affect the scattered intensity (the layer structure factor, the irradiated volume and the polarization of the beam). In particular, we made use of the theoretical calculations of Kabra *et al.* (1986) in order to compute the DXS intensity distribution in the case of the layer-displacement mechanism and the dislocation-based model. The quantitative comparison of experimental and calculated $[10L]_h$ scans revealed that the transformation occurs through the glide of partial dislocations and not by the layer-displacement mechanism. Moreover, we showed that the 3C polytype is indeed unstable at high temperature: partially transformed 3C single crystals subjected to high temperature annealing tend to transform into the 6H polytype. However, we also showed that (almost) defect-free 3C-SiC single crystals remain stable even at temperatures at which they are known to be usually unstable. This apparent stability has probably a kinetic origin, *i.e.* the lack of crystalline defects inhibits the transformation. The wide-range reciprocal space mapping technique appears as a simple and highly quantitative tool to study the defect structure of single crystals undergoing polytypic transformations.

Acknowledgements

D.D. is grateful to the Region Limousin (France) for its financial support. D.C. and I.G-S. thank the MINTEX - French ANR program (contract number ANR-09-BLAN-0189-01) and the MANSiC – Marie Curie Research and Training Network (contract number MRTN-CT-2006-035735) for their financial supports. The following free open-source softwares have been used during the course of this work: the GNU/Linux – Ubuntu operating system, the OpenOffice.org software suite, the Python programming language (associated with the NumPy / SciPy libraries), Inkscape, GIMP and ImageJ. The corresponding developers and communities are gratefully acknowledged.

References

Authier, A. (2001). *Dynamical Theory of X-ray Diffraction*. IUCr Monographs on Crystallography 11. New-York: Oxford University Press.

de Berg, M., Cheong, O., van Kreveld, M., Overmars, M. (2008). *Computational Geometry*. Berlin Heidelberg: Springer-Verlag.

Boulle, A., Masson, O., Guinebretière, R., Dauger, A. (2001). *Appl. Surf. Sci.* **180**, 322-327.

Boulle, A., Masson, O., Guinebretière, R., Lecomte, A., Dauger, A. (2002). *J. Appl. Crystallogr.* **35**, 606-614.

Boulle, A., Conchon, F., Guinebretière, R. (2006). *Acta Crystallogr. A* **62**, 11-20.

Boulle, A., Chaussende, D., Latu-Romain, L., Conchon, F., Masson, O., Guinebretière, R. (2006). *Appl. Phys. Lett.* **89**, 0919021-3.

Boulle, A., Chaussende, D., Conchon, F., Ferro, G., Masson, O., (2008). *J. Cryst. Growth* **310**, 982-987.

Boulle, A., Aube, J., Galben-Sandulache, I., Chaussende, D. (2009). *Appl. Phys. Lett.* **94**, 201904 1-3.

Heine, V., Cheng, C. Needs, R. J. (1992). *Mater. Sci. Eng. B* **11**, 55-60.

Holloway, H. (1969). *J. Appl. Phys.* **40**, 4313-4321.

Jagodzinski, H. (1954) *Acta. Crystallogr.* **7**, 300.

Jagodzinski, H. (1971) *Kristallogr.* **16**, 1235-1246.

Jepps, N. W., Page, T. F. (1983). *Proc. Cryst. Growth Charact.* 7, 259-307.

Kabra, V. K., Pandey, D., Lele, S. (1986). *J. Mater. Sci.* **21**, 1654-1666.

Käckell, P., Furthmüller, J., Bechstedt, F., (1999). *Phys. Rev. B* **60**, 13261-13264.

Knippenberg, W. F. (1963). *Philips Res. Rep.* **18**, 161-274.

Krishna, P., Marshall, R. C. (1971). *J. Cryst. Growth* **11**, 147-150.

Landau, L. (1937). *Phys. Z. SowjUn.* **12**, 579-585.

Lele, S. (1980). *Acta Crystallogr. A* **36**, 584-588.

Lifshitz, I. M. (1937). *Phys. Z. SowjUn.* **12**, 623-643.

Limpijumnong, S., Lambrecht, W. R. L. (1998) *Phys. Rev. B* **57**, 12017-12022.

Lindefelt, U., Iwata, H., Öberg, S., Briddon, P. R. (2003). *Phys. Rev. B* **67**, 155207 1-12.

Masson, O., Boulle, A., Guinebretière, R., Lecomte, A., Dauger, A. (2005). *Rev. Sci. Inst.* **76**, 063912 1-7

Nagasawa, H., Yagi, K., Kawahara, T. (2002). *J. Cryst. Growth* **237-239**, 1244-1249.

Nagasawa, H., Yagi, K., Kawahara, T., Hatta, N. (2006). *Chem. Vap. Deposition* **12**, 502-508.

Nagasawa, H., Abe, M., Yagi, K., Kawahara, T., Hatta, N. (2008). *Phys. Stat. Sol. (b)* **245**, 1272-1280.

Ogbuji, L. U., Mitchell, T. E., Heuer, A. H. (1981). *J. Amer. Ceram. Soc.* **64**, 91-99.

Pandey, D. (1984). *Acta Crystallogr. B* **40**, 567-569.

Pandey, D., Prasad, L., Lele, S., Gauthier, J. P. (1987). *J. Appl. Cryst.* **20**, 84-89.

Pirouz, P. (1989). *Inst. Phys. Conf. Ser.* **104**, 49-56.

Pirouz, P., Yang, J. W. (1993). *Ultramicroscopy* **51**, 189-214.

Polychroniadis, E., Syväjärvi, M., Yakimova, R., Stoemenos, J. (2004). *J. Cryst. Growth* **263**, 68-75.

Püsche, R., Hundhausen, M., Ley, L., Semmelroth, K., Schmid, F., Pensl, G., Nagasawa, H. (2004). *J. Appl. Phys.* **96**, 5569-5575.

Thomas, T., Pandey, D., Waghmare, U. V. (2008). *Phys. Rev. B* **77**, 121203(R) 1-4.

Waasmaier, D., Kirfel, A. (1995). *Acta Crystallogr. A* **51**, 416-431.

Warren, B. E. (1969). *X-Ray Diffraction*. New-York: Addison – Wesley.

Yoo, W. S., Matsunami, H. (1991). *J. Appl. Phys.* **70**, 7124-7131.

Figure caption

Figure 1

(a) schematic representation of a portion of the reciprocal lattice of 3C-SiC (dotted lattice). The accessible reflections are represented as gray spheres (only the reflection in the left-hand side quadrant are indexed). The large half-sphere is the sphere of resolution which limits the area accessible with the X-ray wavelength. The two gray half-spheres correspond to the Laüe zones which can be accessed in the transmission geometry. The red-yellow shaded area is the portion of the reciprocal space that is recorded when the incident beam (indicated by the incident wave-vector $\mathbf{K}_0$) is scanned from $\omega = 1°$ to $\omega = 31°$. The bold 120°-wide arcs correspond to the portion of the Ewald sphere associated with the PSD. The dashed arcs indicate the position of the Ewald sphere when the (-113) and (002) planes come into diffraction. (b) schematic representation of the actual data mesh. Each circle is a measured data point. $\delta\omega$ and $\delta 2\theta$ are the scanning steps.

Figure 2

(a) schematic representation of the cubic (black) and hexagonal (red) lattices. $\mathbf{K}_0$ and $\mathbf{K}_s$ are the incident and scattered wave vectors. ϕ is the asymmetry angle, *i.e.* the angle between the scattering vector $\mathbf{Q} = \mathbf{K}_s - \mathbf{K}_0$ and the normal to the surface of the crystal, $[001]_c$. The 3C-SiC reflections are represented as gray spheres. The direction joining the (002) and (-113) reflections (bold red) corresponds to the $[10L]_h$ row.

(b) typical reciprocal space map of a partially transformed (001)-oriented 3C-SiC single crystal (with a 5.2% transformation level). The diffuse streak joining the (002) and (-113) reflections is clearly visible. The angle $\psi = 54.74°$ is the angle between the {001} and the {111} planes of a cubic lattice.

(c) 12x magnification (in reversed contrast) of the (002) reflection evidencing the two equivalent [-111] and [1-11] streaks and the PSD streak. Notice that despite the fact that a very wide area of the reciprocal space is scanned, high-resolution is achieved.

Figure 3

Plot of the different contributions to the $[10L]_h$ scan. The coherent (dashed line) and diffuse (solid line) are plotted in black (left axis) and the contributions of the structure factor, the irradiated volume and the polarization have *not* been included in the calculation. The curves have been shifted vertically for clarity. The squared structure factor (square), the irradiated volume (triangle) and polarization (circle) are drawn in red (right axis) and have been normalized to unit maximum. The irradiated volume and the structure factor significantly affect the intensity in the range considered, whereas the polarization has a less pronounced effect. The vertical dotted lines indicate the positions of the peaks of 6H-SiC.

Figure 4

Schematic drawing of the diffraction geometry when considering the diffraction from a volume element $dV = Sdz$ located at a depth z below the surface of the crystal. S_0 is the beam cross section and t is the thickness of the crystal. $l_1 + l_2$ is the path length of the beam inside the crystal.

Figure 5

$[10L]_h$ scan in the L = 1.5-2.5 region of a 5.2% - transformed 3C-SiC crystal (x_t = 40%, τ = 13%). Experimental data: black circles; simulation: gray line. The coherent (dashed line) and diffuse (black line) components are also shown (divided by a factor 2 for clarity). The red curves labeled +5% and -5% correspond to a 5% increase or decrease of the transformation level in the transformed areas.

Figure 6

(a) experimental (black line) $[10L]_h$ scan and simulated scans with the dislocation-based mechanism (gray curve) and with layer-displacement mechanism (dashed curve) in the case of partially transformed sample (sample 1, $x_t\tau$ = 1.6%). The arrows point to characteristic features of the diffuse scattering curve that are perfectly reproduced with the dislocation-based model and that are clearly not reproduced with layer-displacement mechanism. The curves are shifted vertically for clarity.

(b) $[10L]_h$ scan from sample 1 annealed at 1700°C for 5h, the transformation level is now $x_t\tau$ = 5.2%. Black line: experimental data; gray line: simulation. The curves are shifted vertically for clarity. The vertical dotted lines indicate the positions of the peaks of 6H-SiC.

Figure 7

(a) $[10L]_h$ scan from sample 2 in its initial state ($x_t\tau$ = 1.6%) and (b) after annealing at 1800°C ($x_t\tau$ = 3.75%). (c) sample 3 in its initial state ($x_t\tau$ = 0.004%) and (d) after annealing at 1800°C and 1900°C ($x_t\tau$ = 0.004%). The vertical dotted lines indicate the positions of the peaks of 6H-SiC.

Fig. 1

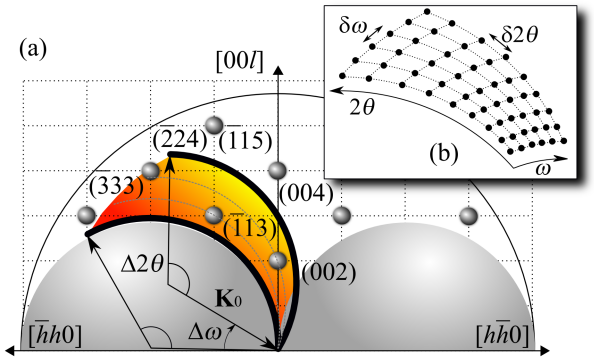

Fig. 2

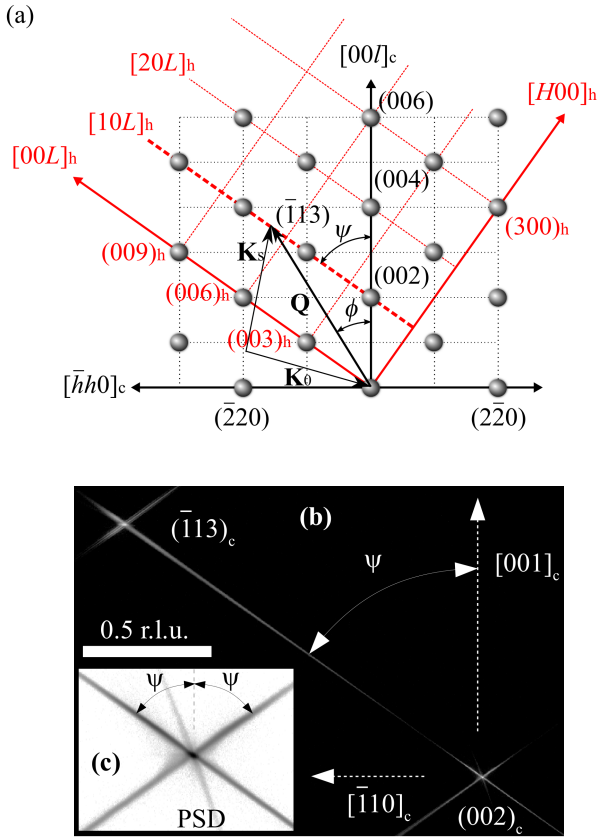
(a)
[20L]h
[00l]c
[H00]h
[10L]h
(006)
[00L]h
(004)
(1̄13)
(300)h
ψ
(009)h
Ks
(002)
(006)h
Q
ϕ
(003)h
[h̄h0]c
K0
(2̄20)
(22̄0)
(b)
(1̄13)c
ψ
[001]c
0.5 r.l.u.
ψ
ψ
(c)
PSD
[1̄10]c
(002)c

Fig. 3

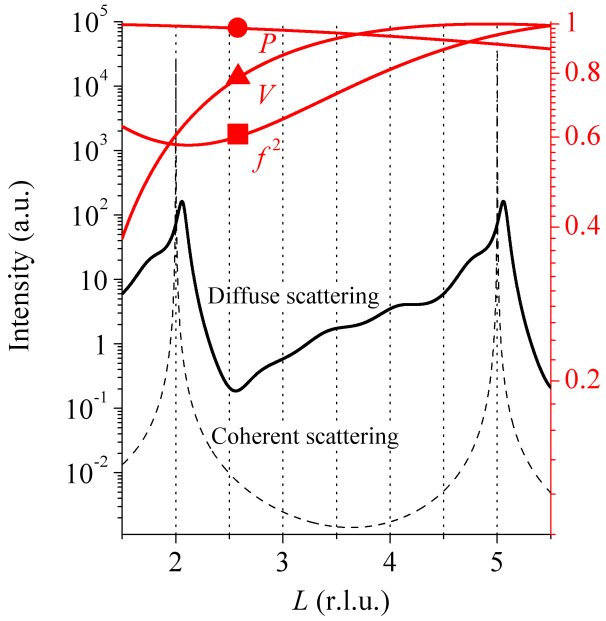
Intensity (a.u.)
10^5
10^4
10^3
10^2
10
1
10^{-1}
10^{-2}
1
0.8
0.6
0.4
0.2
P
V
f^2
Diffuse scattering
Coherent scattering
2
3
4
5
L (r.l.u.)

Fig. 4

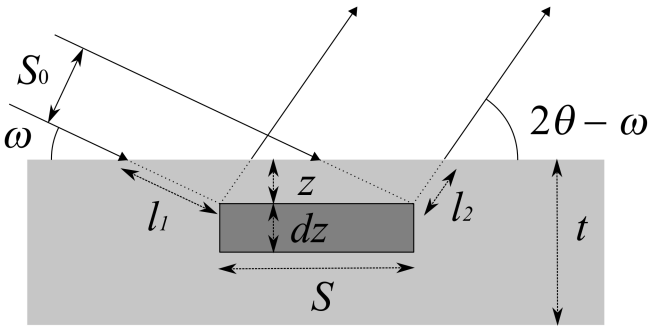

Fig. 5

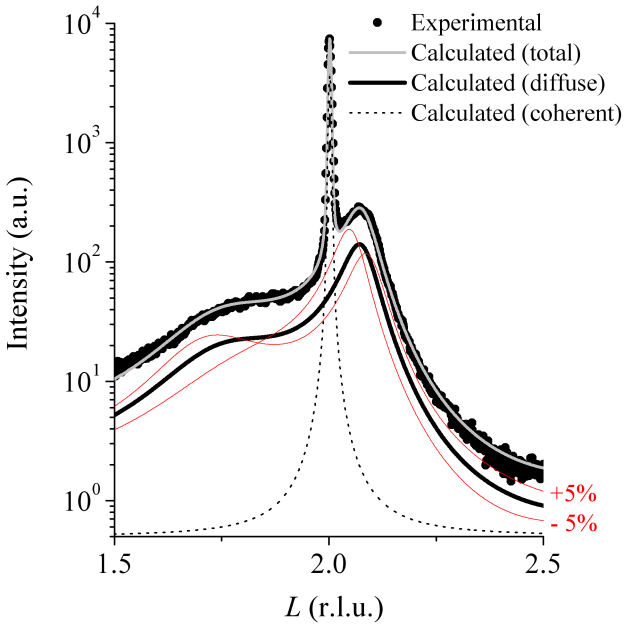
Experimental
Calculated (total)
Calculated (diffuse)
Calculated (coherent)
Intensity (a.u.)
10^4
10^3
10^2
10^1
10^0
+5%
- 5%
1.5
2.0
2.5
L (r.l.u.)

Fig. 6

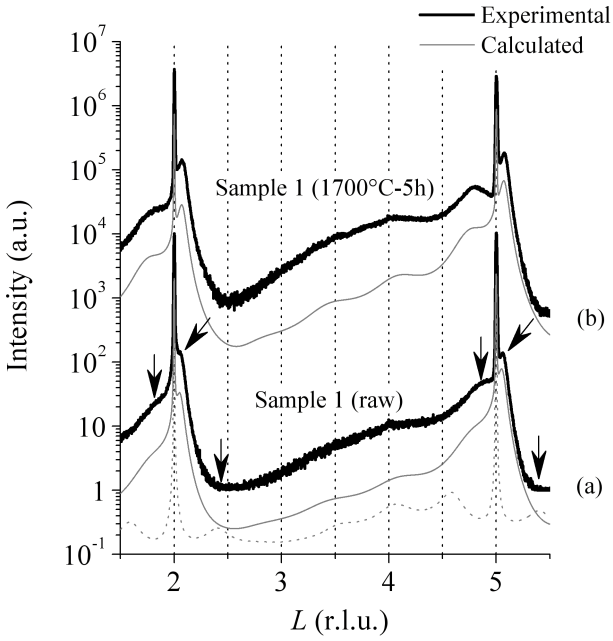
Experimental
Calculated
Intensity (a.u.)
Sample 1 (1700°C-5h)
Sample 1 (raw)
(b)
(a)
L (r.l.u.)

Fig. 7

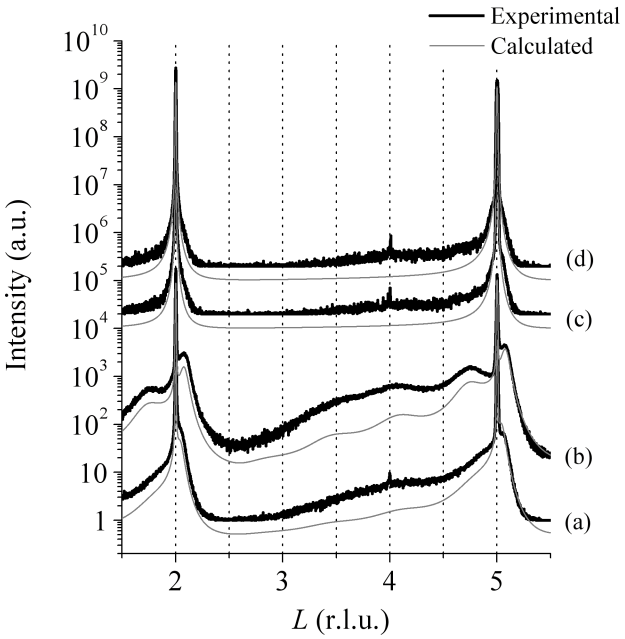
Experimental
Calculated
Intensity (a.u.)
10^{10}
10^{9}
10^{8}
10^{7}
10^{6}
10^{5}
10^{4}
10^{3}
10^{2}
10
1
(d)
(c)
(b)
(a)
2
3
4
5
L (r.l.u.)